Editors' Suggestion

Energy Dissipation of Fast Electrons in Polymethylmethacrylate: Toward a Universal Curve for Electron-Beam Attenuation in Solids between ∼0 eV and Relativistic Energies

Wolfgang S. M. Werner,* Florian Simperl, Felix Blödorn, Julian Brunner, and Johannes Kero
Institut für Angewandte Physik, Technische Universität Wien, Wiedner Hauptstraße 8-10/E134, A-1040 Vienna, Austria

Alessandra Bellissimo
Institut für Photonik, Technische Universität Wien, Gußhausstraße 27-29/E387, A-1040 Vienna, Austria

Olga Ridzel
Theiss Research, 7411 Eads Avenue, La Jolla, California 92037-5037, USA

(Received 28 November 2023; revised 20 February 2024; accepted 2 April 2024; published 1 May 2024)

Spectroscopy of correlated electron pairs was employed to investigate the energy dissipation process, as well as the transport and the emission of low-energy electrons on a polymethylmethacrylate surface, providing secondary electron spectra causally related to the energy loss of the primary. Two groups are identified in the cascade of slow electrons, corresponding to different stages in the energy dissipation process. The characteristic lengths for attenuation due to collective excitations and momentum relaxation are quantified for both groups and are found to be distinctly different: $\lambda_1 = (12 \pm 2)$ Å and $\lambda_2 = (62 \pm 11)$ Å. The results strongly contradict the commonly employed model of exponential attenuation with the electron inelastic mean free path as characteristic length, but they essentially agree with a theory used for decades in astrophysics and neutron transport, albeit with characteristic lengths expressed in units of angstroms rather than light-years.

DOI: 10.1103/PhysRevLett.132.186203

Electrons with energies in the range of ∼0–20 eV in vacuum are playing an increasingly important role in modern science and technology. While low-energy electrons (LEEs) have been utilized for a century in electron microscopy [1], modern applications of nanotechnology require an improved understanding of the energy dissipation of LEEs near solid surfaces. This concerns the effective interaction volume in electron-beam lithography caused by electron diffusion (proximity effect) [2–5], as well as focused electron-beam deposition [6], spacecraft surface charging [7], electron cloud formation in charged particle storage rings [8,9], astrochemistry [10], and plasma-wall interaction in fusion research [11]. LEEs are also the essential agents for DNA strand breaks as a result of the irradiation of biological tissue with ionizing radiation [12]. The transport of LEEs near solid surfaces is particularly important for the emerging fields of plasmonics [13] and photonics [14–17].

For medium energies (∼100 eV–100 keV), the electron-solid interaction relevant to electron spectroscopy for surface analysis is nowadays quantitatively understood [18–22]. At low energies (< 100 eV), however, it is still not possible to satisfactorily describe essential observables upon the impact of a primary electron, such as the spectrum of emitted secondary electrons (SEs) or the SE yield, since additional physical phenomena come into play that make the parameters of theoretical models less reliable, while experiments with LEEs are generally more difficult [23]. The refinement of any model is complicated by the lack of benchmark experiments specifically designed to obtain information on individual physical parameters or processes. The main idea of the present approach is to use the quantitative model for medium energies to obtain information on the (poorly understood) low-energy range by using medium energy primary electrons as messengers of the depth of creation of low energy secondaries. The attenuation law is then quantified by analysis of the SE intensity as a function of the depth of creation.

Concerning the length scale over which low-energy electrons are attenuated, many authors adopt the same

approach as for medium energies—i.e., exponential attenuation, with the inelastic mean free path (IMFP) as the characteristic length. We challenge this approach for low energies. The energy dissipation of fast electrons is investigated in polymethylmethacrylate (PMMA), a photoresist commonly used in electron-beam lithography [2,3,24,25], and study the transport and emission of LEEs liberated upon the impact of the primary. Correlated electron pairs of primary (medium-energy) electrons striking a surface and secondary (low-energy) electrons emitted as a result are measured in coincidence, yielding secondary electron spectra causally related to a given energy loss of the primary after a certain number of inelastic collisions. We then obtain information about the *low-energy* electron transport by invoking the quantitative model for the *medium-energy* range [18,20,21] to calculate the average depth at which a given number of energy losses of the primaries take place. Note that this procedure is also followed in attosecond physics to quantify photoelectron delay times due to collective excitations near solid surfaces [26]. We assume that the average number, α, of electrons liberated by each energy loss is unity [27,37–40]. Then, comparison of the intensity of energy losses of the primary—i.e., the number of secondary electrons *created at a certain depth* with the number *emitted into vacuum*—provides the length scale over which low-energy secondary electrons are attenuated.

The results strongly contradict the commonly used exponential attenuation law. This is not unexpected, given the dynamic interplay between energy fluctuations arising from collective excitations (governed by λ_i, the IMFP) and momentum relaxation attributed to elastic scattering by the Coulomb potential of the ionic cores [described by the transport mean free path (λ_{tr}, TrMFP) [41]]. This relationship changes dramatically at energies below 100 eV. A universal attenuation law accounting for these phenomena developed in astrophysics [42–44] describes our results satisfactorily. The chain of processes we identify in the energy dissipation mechanism is expected to be more generally encountered—e.g., in biological matter exposed to ionizing radiation [12] and energies extending into the relativistic range, where plasmon excitation is still the dominant energy-loss mechanism [41].

The spectra of electron pairs correlated in time were measured for electrons with energies of $E_0 = 173$, 500, and 1000 eV incident on a PMMA surface (see [28] for experimental details). Figure 1(a) shows the raw data for $E_0 = 500$ eV on a false color scale. Each pixel in the double-differential coincidence data in Fig. 1(a) represents the intensity of detected electron pairs: a fast, inelastically scattered (primary) electron with energy E_1, and a slow secondary electron with energy E_2 created during the impact of the primary. On a simple model for the SE emission process [see Fig. 1(b)], the energy loss $\Delta E = E_0 - E_1$ of a primary electron is transferred to an occupied

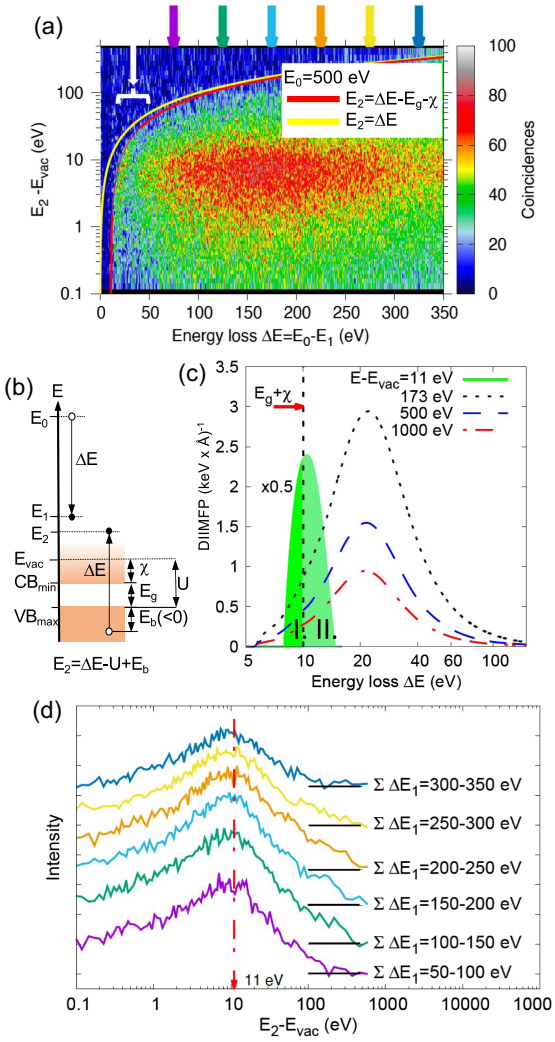

FIG. 1. (a) Double-differential secondary electron-electron energy-loss coincidence spectrum (SE2ELCS) for $E_0 = 500$ eV electrons striking a PMMA surface. The red curve indicates the maximum energy in vacuum for an emitted electron created by an energy loss ΔE of the primary. (b) Schematic illustration of the electronic structure. (c) Differential inverse inelastic mean free path (DIIMFP) for PMMA for energies of 11, 173, 500, and 1000 eV above the vacuum level [47]. The maximum energy loss for 11 eV electrons (above vacuum) is seen to be 15.5 eV, since no allowed states exist at energies below $E_{vac} - \chi$. (d) SE spectra obtained by integrating the data in (a) over the indicated ranges of ΔE [see the arrows in (a)].

state in the valence band with (negative) binding energy E_b. The secondary electron liberated inside the solid can be emitted into vacuum if its energy suffices to overcome the surface barrier $U = E_g + \chi$ [45] consisting of the energy gap, $E_g = 5.5$ eV, and the electron affinity, $\chi = 4.5$ eV [46]. The red curve in Fig. 1(a) delimits the maximum energy in vacuum of a secondary electron created by a given energy loss $E_2 = \Delta E - U$.

Just below the red curve in Fig. 1(a), at energies near the plasmon resonance of $\hbar\omega_p \sim 21$ eV [see Fig. 1(c)], the

region of high intensity indicated by the white arrow is attributable to a plasmon-assisted (e,2e) process [37–40]. Multiple plasmon excitation by the primary is responsible for the intensity at larger losses (> 30 eV). Here, the intensity along the E_2 axis approximately peaks at $E_2 - E_{\mathrm{vac}} = \hbar\omega_p - U \sim 11$ eV [48], in a process where a plasmon decays and the resonance energy is transferred to a single [27,37–40] solid-state electron in the valence band that overcomes the surface barrier. The differential inverse inelastic mean free path (DIIMFP) is shown for various energies in Fig. 1(c). For projectile energies well above the plasmon resonance, the shape of the DIIMFP is practically identical, explaining the similarity of the coincidence SE spectra for arbitrary energy-loss ranges in the course of multiple plasmon excitation [Fig. 1(d)]. These observations provide further evidence for the Markov-type character of multiple inelastic electron scattering leading to SE emission [49].

The intensity of coincidences along ΔE in Fig. 1(a) is remarkable, in that it increases monotonically up to an energy of ~150 eV and decreases afterwards. A similar behavior was observed for all primary energies and can be seen more clearly for 1000 eV in Fig. 2: while the intensity in the singles energy-loss spectrum [Fig. 2(a)] decreases monotonically with the energy loss, the total number of emitted SEs [i.e., the coincidence data integrated over E_2, Fig. 2(b)] exhibits a maximum at $\Delta E \sim 250$ eV.

The electron energy-loss spectrum is a superposition of the n-fold self-convolutions of the DIIMFP [18,50]. Fitting the spectra to a linear combination of such functions then yields the contribution of n-fold inelastically scattered primaries to the spectrum [18,41]. The corresponding fits are shown as black curves in Figs. 2(a) and 2(b), while the colored filled curves represent the contributions to the spectra of individual n-fold plasmon losses. The areas under these curves correspond, respectively, to the number of inelastic collisions experienced by the primaries (for the singles spectrum) and the number of secondary electrons emitted as a result (for the coincidence spectrum). These quantities are referred to as partial intensities, C_n [51]. The reduced partial intensities, $\gamma_n = C_n/C_1$, are presented in Fig. 2(c).

For the first few scattering orders, the singles partial intensities are close to unity. It is then expected that the coincidence partial intensities should follow the relationship $\gamma_n^{\mathrm{coi}} = n$ [green line in Fig. 2(c)], since n energy losses create n secondary electrons. However, all coincidence partial intensities consistently lie below the green line. The probability for n-fold scattering increases with the traveled path length [52]—i.e., the average depth at which higher-order collisions take place increases monotonically with the collision number. Then, the decrease of the number of emitted secondary electrons with increasing scattering order—i.e., the deviation of the coincident intensity from the expected behavior $\gamma_n^{\mathrm{coi}} = n$—is attributable to a corresponding increase of the depth of creation $\langle z_n \rangle$.

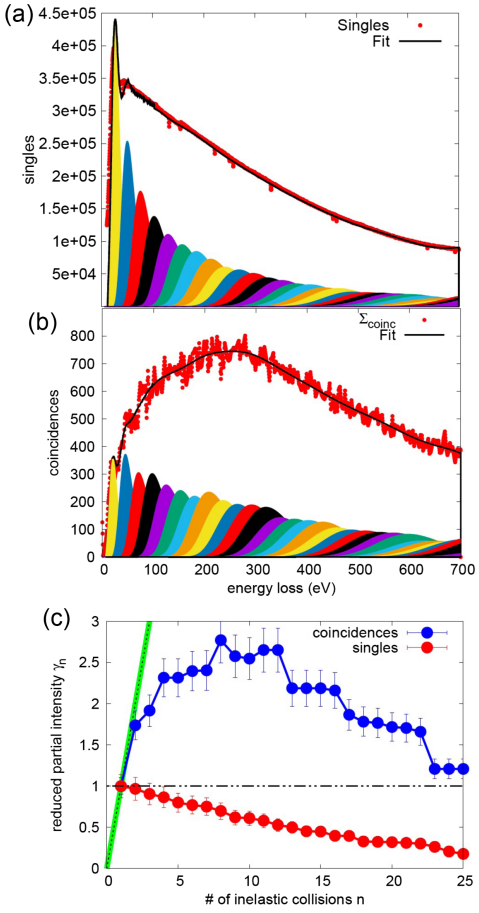

FIG. 2. (a) Red data points show the singles energy-loss spectra (acquired during the coincidence run) for a primary energy of $E_0 = 1000$ eV. (b) Corresponding coincidence spectra, obtained by integrating the double-differential data over E_2. Black curves are a fit of these data to a linear combination of multiple self-convolutions of the DIIMFP, shown by the filled colored curves. (c) Reduced partial intensities $\gamma_n = C_n/C_{n=1}$, where the quantities C_n are the areas under the filled curves for the spectra shown in (a) and (b). The green line represents the identity $\gamma_n = n$.

At this stage, we invoke the quantitative model for medium-energy electron-solid interaction [20,21] to calculate the average depth $\langle z_n \rangle$ at which n-fold scattering of the primaries takes place using a Monte Carlo (MC) model (see the Supplemental Material [28]). Since n-fold scattering leads to the generation of n secondary electrons at the corresponding depths, the quantity $\gamma_n^{\mathrm{coi}}/(n \times \gamma_n^{\mathrm{sing}})$ as a function of $\langle z_n \rangle$ describes the attenuation of SEs created at a certain depth before they reach the surface. These attenuation curves are shown in Fig. 3(a) on a semilogarithmic scale. The accessible depth ranges are widely different for the three considered primary energies, but their depth dependence is satisfactorily described by the same attenuation law, which is clearly not a simple exponential function: the solid (red) curves represent a fit to a double exponential function,

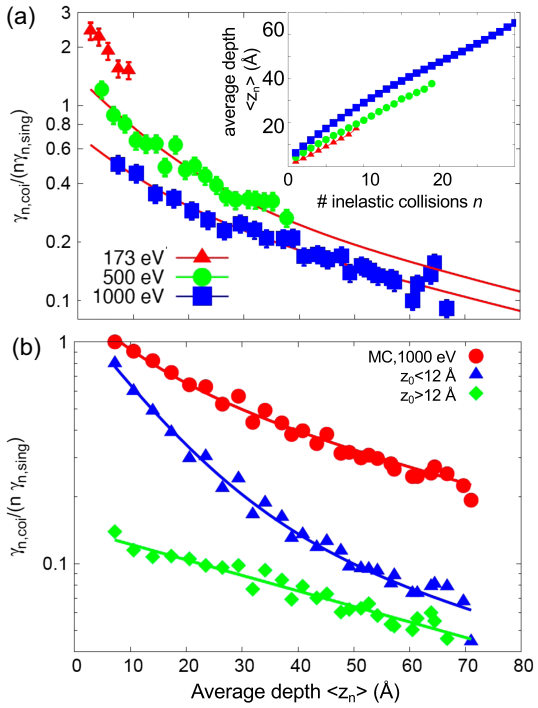

FIG. 3. (a) Experimental attenuation curves of the SE yield as a function of depth, $\gamma_n^{\mathrm{coi}}/(n \times \gamma_n^{\mathrm{sing}})(\langle z \rangle)$, for primary energies of 173, 500, and 1000 eV. The red solid curves represent a fit to a double exponential function [Eq. (1)]. The inset shows the MC results for the average depth $\langle z_n \rangle$ at which, on average, n inelastic collisions of the primaries occur. (b) MC simulation of the results shown in (a) for 1000 eV (see text). The data in (a) and (b) were offset by multiplication to improve the distinguishability of individual curves.

$$\alpha_1 \exp(-z/\lambda_1) + \alpha_2 \exp(-z/\lambda_2), \tag{1}$$

yielding distinctly different characteristic lengths of $\lambda_1 = (12 \pm 2)$ Å and $\lambda_2 = (62 \pm 11)$ Å.

The same analysis was applied to simulated spectra from our MC model [28]. The MC results for 1000 eV are shown by the red circles in Fig. 3(b), along with a fit (solid red curve) to a double exponential curve with the same characteristic lengths λ_1 and λ_2 as in Fig. 3(a). The blue and green points are for subsets of these data for depths of origin z_0 smaller (triangles, blue) and larger than 12 Å (diamonds, green). The solid blue curve is a double exponential function with the same characteristic lengths as above, while the solid green curve is a single exponential function with characteristic length λ_2. The MC calculations also yield the mean energies in vacuum of the above two groups as $\langle E_{\lambda_1} \rangle = 11$ eV and $\langle E_{\lambda_2} \rangle = 4$ eV.

These results suggest a rather simple chain of processes for the first stages of energy dissipation: Multiple plasmon excitation of the fast primary electron leads to the creation of secondaries with an energy distribution peaking around $\hbar\omega_p - U \sim 11$ eV. During the transport to the surface, such an electron has a significant probability to undergo an inelastic collision: the area under the curves for 11 and 1000 eV in Fig. 1(c) is of the same order of magnitude. Hence, the corresponding characteristic length (denoted by λ_1 in the following) will be small. If such a first-generation "11 eV" secondary electron is created at a depth larger than λ_1 (green diamonds, $z_0 > 12$ Å), it is likely to suffer another energy loss before escape. In case this energy loss is smaller than the surface barrier [$\Delta E < U$; see region I in the 11 eV DIIMFP in Fig. 1(c)] and is transferred to an electron in the valence band, the latter (liberated) electron can only be promoted to a hot-electron state in the conduction band below the vacuum level. It cannot escape into vacuum. The inelastically scattered electron itself will have an energy just above the vacuum level after the collision.

The other case when the energy loss of the first-generation secondary electron exceeds the surface barrier [$\Delta E > U$; region II in Fig. 1(c)] leads to a situation where in the final state, the roles of the scattered and liberated electrons are reversed: the scattered electron will be a hot electron below the vacuum level, while the liberated electron will have an energy above the vacuum level and can escape. In both cases, the energy of the emitted electron with a positive energy in vacuum will be small (typically of the order of a few eV above vacuum), and its IMFP will be large due to the limited availability of final states in further scattering processes. Hence, the characteristic length for attenuation (λ_2) will be large. Then, the attenuation curve should be a single exponential with characteristic length λ_2.

If a first-generation "11 eV" electron is created at a depth smaller than λ_1 (blue triangles, $z_0 < 12$ Å), it can escape without further loss if its initial direction points outward; otherwise, it will scatter and belong to the λ_2 group thereafter, resulting in a double exponential attenuation curve. The mechanism outlined above corresponds exactly to the results shown in Fig. 3(b).

In the framework of linear transport theory, the expression for the effective attenuation length (EAL), λ_a, that takes into account the combined influence of energy fluctuations (inelastic scattering) and momentum relaxation (deflections), is given by [42–44,53]

$$\lambda_a = \frac{\lambda_i \lambda_{\mathrm{tr}}}{\lambda_i + \lambda_{\mathrm{tr}}} \nu_0 = \lambda_{\mathrm{tr}} c \nu_0, \tag{2}$$

where the single scattering albedo is given by $c = \lambda_i/(\lambda_i + \lambda_{\mathrm{tr}})$ and the quantity ν_0 is the positive root of the characteristic equation

$$\frac{2}{c} = \nu_0 \ln \frac{\nu_0 + 1}{\nu_0 - 1}. \tag{3}$$

In the medium-energy range, the TrMFP exceeds the IMFP by a significant factor, yielding a value for ν_0 very close to unity, and the EAL is slightly smaller than the

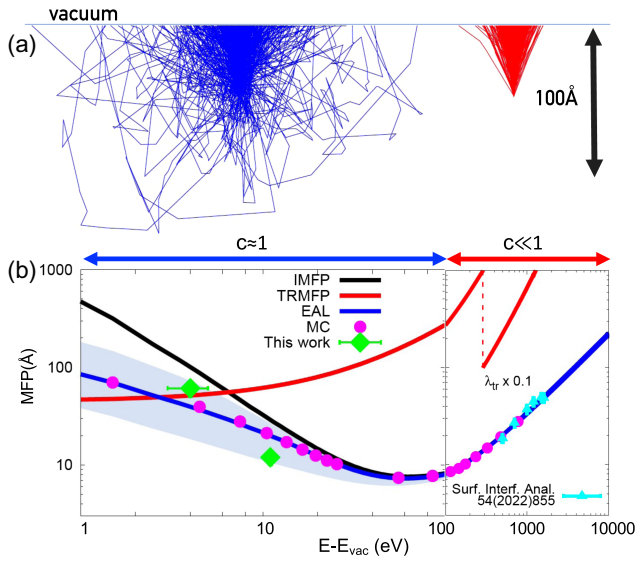

FIG. 4. (a) Trajectories of electrons emitted isotropically at a depth of 50 Å and reaching the surface without energy loss. Left (blue): Single scattering albedo $c \approx 1$. Right (red): $c \ll 1$. (b) Electron inelastic mean free path (IMFP, black [54]), transport mean free path (TrMFP, red), and effective attenuation length [EAL, blue, Eq. (2)]. The (magenta) circles are the results of MC model calculations for the EAL, and the (cyan) triangles are earlier experimental data for the IMFP [22]. The green diamonds represent the results for $\lambda_{1,2}$ derived from the data in Fig. 3(a). The blue shaded region represents the uncertainty in the EAL when the TrMFP is increased/decreased by a factor of 3.

IMFP, the difference being ~10% or less. For small values of $c \ll 1$, the particle will move along an approximately straight line, and the attenuation is dominated by the IMFP [see Fig. 4(a)]. For low energies, as the TrMFP assumes values of the order of the IMFP or less and the influence of momentum relaxation becomes more pronounced, the EAL and IMFP are essentially different. For values of $c \sim 1$, many deflections occur before an inelastic process takes place.

Identifying $\langle E_{\lambda_{1,2}} \rangle$ as the energies associated with the characteristic lengths of the two stages of the energy dissipation process, $\lambda_{1,2}$ are shown as green diamonds in Fig. 4(b) and are compared with the mean free path for inelastic scattering λ_i (IMFP [54]) and momentum relaxation λ_{tr} (TrMFP [55]), as well as the effective attenuation length λ_a according to Eq. (2).

The (magenta) circles in Fig. 4 were calculated with the MC technique and agree quantitatively with Eq. (2). The present results for λ_1 and λ_2 differ by more than a factor of 2 from the IMFP and agree significantly better with Eq. (2), underscoring the importance to adequately account for the combined influence of collective excitations and momentum relaxation.

In summary, the energy dissipation process of fast electrons in PMMA begins with multiple plasmon excitation of the primary. Plasmon decay induces interband transitions acting as sources of SEs, most of them with an energy of ~11 eV above the vacuum level, since the DIIMFP for any projectile energy above the plasmon resonance has its maximum at $\Delta E \sim 21$ eV [Fig. 1(c)]. The subsequent scattering process leads to a secondary electron (and a hot electron) just above (below) the vacuum level, making up the low-energy part of the cascade.

The characteristic lengths of these two groups of electrons have been determined by using the quantitative model for medium energies to obtain information about the low-energy transport. Comparison of the characteristic length $\lambda_{1,2}$ with the universal curve, Eq. (2), suggests that the transport of low-energy electrons can be described by the same physical law as used in light scattering in interplanetary nebulae, impressively demonstrating the scaling of physical laws over 26 orders of magnitude. The scientific debate on low-energy electron attenuation [56–58] should explore the merits of linear transport theory at the earliest stage possible.

The authors would like to thank Drs. C. J. Powell and S. Tanuma for helpful discussions and for making their IMFP data available to us. The computational results have been achieved using the Vienna Scientific Cluster (VSC). Financial support by the Horizon 2022 Marie-Curie Actions Initial Training Network (ITN) EUSpeclab (Grant No. 101073486) and by the FP7 People: Marie-Curie Actions Initial Training Network (ITN) SIMDALEE2 (Grant No. PITN 606988) is gratefully acknowledged.

*werner@iap.tuwien.ac.at

[1] J. Goldstein, D. E. Newbury, P. Echlin, D. C. Joy, A. D. Romig, C. E. Lyman, C. Fiori, and E. Lifshin, *Scanning Electron Microscopy and X-ray Microanalysis* (Plenum, New York and London, 1992).
[2] T. Kozawa and S. Tagawa, Jpn. J. Appl. Phys. **49**, 030001 (2010).
[3] T. Kozawa and T. Tamura, Jpn. J. Appl. Phys. **60**, 126504 (2021).
[4] J. Torok, B. Srivats, S. Memon, H. Herbol, J. Schad, S. Das, L. Ocola, G. Denbeaux, and R. L. Brainard, J. Photopolym. Sci. Technol. **27**, 611 (2014).
[5] M. Ossiander, M. L. Meretska, H. K. Hampel, S. W. D. Lim, N. Knefz, T. Jauk, F. Capasso, and M. Schultze, Science **380**, 59 (2023).
[6] M. Huth, F. Porrati, C. Schwalb, M. Winhold, R. Sachser, M. Dukic, J. Adams, and G. Fantner, Beilstein J. Nanotechnol. **3**, 597 (2012).
[7] H. B. Garrett and A. C. Whittlesey, *Guide to Mitigating Spacecraft Charging Effects* (Wiley-Blackwell, New York, 2012).
[8] R. Cimino, I. R. Collins, M. A. Furman, M. Pivi, F. Ruggiero, G. Rumolo, and F. Zimmermann, Phys. Rev. Lett. **93**, 014801 (2004).
[9] K. Ohmi, Phys. Rev. Lett. **75**, 1526 (1995).

[10] J. H. Bredehöft, E. Böhler, F. Schmidt, T. Borrmann, and P. Swiderek, ACS Earth Space Chem. **1**, 50 (2017).

[11] J. Schou, *Physical Processes of the Interaction of Fusion Plasmas with Solids* (Academic Press, London, 1996), p. 177.

[12] B. Boudaiffa, P. Cloutier, D. Hunting, M. A. Huels, and L. Sanche, Science **287**, 1658 (2000).

[13] S. A. Maier, M. L. Brongersma, P. G. Kik, S. Meltzer, A. A. G. Requicha, and H. A. Atwater, Adv. Mater. **13**, 1501 (2001).

[14] A. L. Cavalieri, N. Müller, T. Uphues, V. S. Yakovlev, A. Baltuska, B. Horvath, B. Schmidt, L. Blümel, R. Holzwarth, S. Hendel *et al.*, Nature (London) **449**, 1029 (2007).

[15] M. Schultze, M. Fieľy, N. Karpowicz, J. Gagnon, M. Korbman, M. Hofstetter, S. Neppl, A. L. Cavalieri, Y. Komninos, T. Mercouris *et al.*, Science **328**, 1658 (2010).

[16] R. Signorell, Phys. Rev. Lett. **124**, 205501 (2020).

[17] A. H. Zewail, J. Phys. Chem. A **104**, 5660 (2000).

[18] W. S. M. Werner, Front. Mater. **10**, 1202456 (2023).

[19] A. Jablonski and C. J. Powell, J. Phys. Chem. Ref. Data **49**, 033102 (2020).

[20] C. J. Powell and A. Jabłonski, J. Phys. Chem. Ref. Data **28**, 19 (1999).

[21] W. S. M. Werner, C. Ambrosch-Draxl, and K. Glantschnig, J. Phys. Chem. Ref. Data **38**, 1013 (2009).

[22] W. S. M. Werner, F. Helmberger, M. Schürrer, O. Ridzel, M. Stöger-Pollach, and C. Eisenmenger-Sittner, Surf. Interface Anal. **54**, 855 (2022).

[23] A. Bellissimo, Ph.D. thesis, Università degli Studi Roma Tre, 2019, http://hdl.handle.net/2307/40933.

[24] R. Pal, A. K. Sikder, K. Saito, A. M. Funston, and J. R. Bellare, Polym. Prepr. **8**, 6917 (2017).

[25] R. Willis and D. Skinner, Solid State Commun. **13**, 685 (1973).

[26] C. Lemell, S. Neppl, G. Wachter, K. Tőkési, R. Ernstorfer, P. Feulner, R. Kienberger, and J. Burgdörfer, Phys. Rev. B **91**, 241101(R) (2015).

[27] Any alternative choice of α leads to rescaling of the vertical axis in Fig. 3 (replacing n with αn in the denominator of the plotted quantity). This does not affect the further analysis in any way (see also [28]).

[28] See Supplemental Material at http://link.aps.org/supplemental/10.1103/PhysRevLett.132.186203 for the present article, which includes Refs. [29–36] for additional information about the experimental procedure, as well as the simulation model.

[29] V. Astašauskas, A. Bellissimo, P. Kuksa, C. Tomastik, H. Kalbe, and W. S. M. Werner, J. Electron Spectrosc. Relat. Phenom. **241**, 146829 (2020).

[30] E. Jensen, R. A. Bartynski, S. L. Hulbert, and E. D. Johnson, Rev. Sci. Instrum. **63**, 3013 (1992).

[31] P. Schattschneider and W. S. M. Werner, J. Electron Spectrosc. Relat. Phenom. **143**, 81 (2005).

[32] W. S. M. Werner and P. Schattschneider, J. Electron Spectrosc. Relat. Phenom. **143**, 65 (2005).

[33] E. Tosatti and G. P. Parravicini, J. Phys. Chem. Solids **32**, 623 (1971).

[34] B. Da, H. Shinotsuka, H. Yoshikawa, and S. Tanuma, Surf. Interface Anal. **51**, 627 (2019).

[35] T. Boutboul, A. Akkerman, A. Breskin, and R. Chechik, J. Appl. Phys. **79**, 6714 (1996).

[36] Z. Ding and R. Shimizu, Surf. Sci. **222**, 313 (1989).

[37] W. S. M. Werner, A. Ruocco, F. Offi, S. Iacobucci, W. Smekal, H. Winter, and G. Stefani, Phys. Rev. B **78**, 233403 (2008).

[38] W. S. M. Werner, F. Salvat-Pujol, A. Bellissimo, R. Khalid, W. Smekal, M. Novak, A. Ruocco, and G. Stefani, Phys. Rev. B **88**, 201407(R) (2013).

[39] A. Bellissimo, G.-M. Pierantozzi, A. Ruocco, G. Stefani, O. Y. Ridzel, V. Astašauskas, W. S. M. Werner, and M. Taborelli, J. Electron Spectrosc. Relat. Phenom. **241**, 146883 (2020).

[40] W. S. M. Werner, V. Astašauskas, P. Ziegler, A. Bellissimo, G. Stefani, L. Linhart, and F. Libisch, Phys. Rev. Lett. **125**, 196603 (2020).

[41] W. S. M. Werner, Surf. Interface Anal. **31**, 141 (2001).

[42] K. M. Case and P. F. Zweifel, *Linear Transport Theory* (Addison-Wesley, Reading, MA, 1967).

[43] S. Chandrasekhar, *Radiative Transfer* (Dover Publications, New York, 1960).

[44] B. Davison, *Neutron Transport Theory* (Oxford University Press, Oxford, 1955).

[45] A. Kahn, Mater. Horiz. **3**, 7 (2015).

[46] F. Simperl, F. Blödorn, J. Brunner, W. S. Werner, A. Bellissimo, and O. Ridzel [Phys. Rev. B] (to be published).

[47] O. Y. Ridzel, H. Kalbe, V. Astašauskas, P. Kuksa, A. Bellissimo, and W. S. M. Werner, Surf. Interface Anal. **54**, 487 (2022).

[48] Concerning the surprising fact that the maximum in the SE spectra in Fig. 1(b) is found at a rather high energy of 11 eV, it should be kept in mind that these data constitute SE spectra emitted as a result of a specific energy-loss mechanism, which is discriminated by means of the coincidence technique. The maximum of the SE peak in the singles spectra is located at ∼3.7 eV.

[49] W. S. M. Werner, F. Salvat-Pujol, W. Smekal, R. Khalid, F. Aumayr, H. Störi, A. Ruocco, F. Offi, G. Stefani, and S. Iacobucci, Appl. Phys. Lett. **99**, 184102 (2011).

[50] R. F. Egerton, *Electron Energy Loss Spectroscopy in the Electron Microscope* (Plenum, New York and London, 1985).

[51] ISO 18115-1, Surface Chemical Analysis Vocabulary Part 1, General Terms and Terms Used in Spectroscopy, International Organization for Standardization (2010), https://www.iso.org/obp/ui/en/#iso:std:iso:18115:-1:ed-3:v1:en.

[52] W. S. M. Werner, Phys. Rev. B **55**, 14925 (1997).

[53] I. S. Tilinin and W. S. M. Werner, Phys. Rev. B **46**, 13739 (1992).

[54] H. Shinotsuka, S. Tanuma, and C. J. Powell, Surf. Interface Anal. **49**, 238 (2022).

[55] F. Salvat, A. Jablonski, and C. J. Powell, Comput. Phys. Commun. **165**, 157 (2005).

[56] J. D. Bourke and C. T. Chantler, Phys. Rev. Lett. **104**, 206601 (2010).

[57] P. de Vera and R. Garcia-Molina, J. Phys. Chem. C **123**, 2075 (2019).

[58] D. Geelen, J. Jobst, E. E. Krasovskii, S. J. van der Molen, and R. M. Tromp, Phys. Rev. Lett. **123**, 086802 (2019).